Available at www.ComputerScienceWeb.com
POWERED BY SCIENCE DIRECT®

Pattern Recognition Letters 24 (2003) 791–800

Pattern Recognition Letters

www.elsevier.com/locate/patrec

Joint image registration and volume reconstruction for 3D ultrasound

João M. Sanches *, Jorge S. Marques

Instituto Superior Tecnico/ISR, Avenue Rovisco Pais, 1049-001Lisbon, Portugal

Abstract

Three-dimensional (3D) ultrasound aims to reconstruct a 3D volume of data from a set of ultrasound images. To achieve this goal, accurate measurements of the probe position and orientation are required. This is not always possible in practice, due to the limitation of current spatial location systems. Unfortunately, position errors produce a misalignment of the volume cross-sections which blur the reconstruction results.

To overcome this difficulty an alignment algorithm must be derived. This paper describes a method which performs both tasks: volume reconstruction and image alignment. The proposed algorithm is based on the optimization of a single objective function which depends on both sets of parameters. Reconstruction results with synthetic and medical data are presented showing significant improvement compared to the results obtained with standard technique without alignment.

Keywords: Alignment; Image reconstruction; Medical imaging; Multiplicative noise

1. Introduction

This paper address the problem of volume reconstruction from a sequence of ultrasound images. These images correspond to cross-sections of the human body obtained at different positions of the ultrasound probe (see Fig. 1).

The volume to be inspected is sampled by sweeping the probe providing information about the acoustic properties of the tissues and underlying anatomy (Quistgaard, 1997). There is a spatial locator coupled with the ultrasound probe which gives the position and orientation of the probe for each cross-section of the data sequence (see Fig. 2). From this information, a Three-dimensional (3D) function describing the acoustic properties of the inspected volume is to be estimated.

3D reconstruction of the human anatomy is currently a common procedure in several modalities such as computed tomography (CT) (Herman and Kuba, 1999), magnetic resonance imaging (MRI), positron emission tomography (PET) (Anderson, 1997) and single photon emission computed tomography (SPECT) (Green, 1990). In ultrasound imaging this approach is much less used (Ogawa et al., 1998; Nelson et al., 1999; Nelson and Pretorius, 1997) due to four main reasons (Rohling et al., 1999): (1) the use of non-parallel inspection

* Corresponding author. Tel.: +351-1-841-8195.
E-mail address: jmrs@alfa.ist.utl.pt (J.M. Sanches).

0167-8655/03/$ - see front matter
PII: S0167-8655(02)00182-4

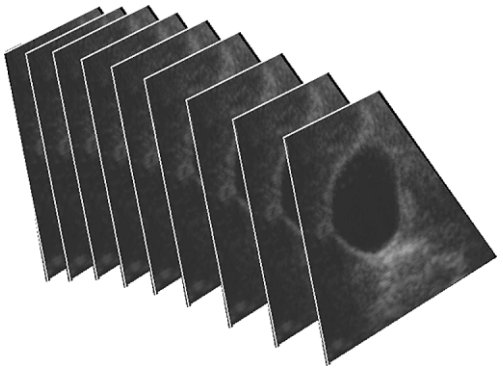

Fig. 1. Ultrasound sequence.

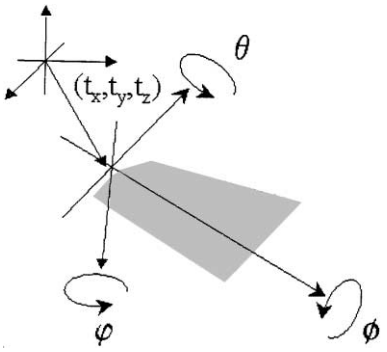

Fig. 2. Position and orientation of the inspection plane.

planes due to free hand probe manipulation, (2) tissue deformations during the acquisition process, (3) sensor position errors (Carr, 1996) and (4) low signal to noise ratio. In fact, in free-hand ultrasound the probe is in full contact with the human body: it is moved and kept under pressure by the medical doctor. This procedure modifies the organs shapes and positions during the acquisition process. Consequently, significant geometric distortions can be observed in ultrasound images. Furthermore, the spatial locator system coupled to the ultrasound probe also introduces significant errors in the position and orientation measurements (see Fig. 3). Some actions can be performed

[1] A minimum amount of pressure is needed however to guarantee a good acoustic coupling between the ultrasound probe and the human body.

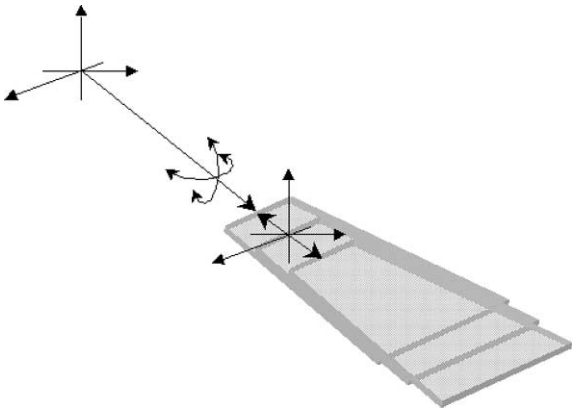

Fig. 3. Position and orientation errors.

to alleviate these difficulties, e.g., by improving accuracy of the spatial locator or by reducing the pressure of the ultrasound probe against the human body. [1] However, to achieve good results, an alignment procedure must be devised.

In this paper a new approach is proposed to compensate the misalignment and geometric distortions introduced during the acquisition process (Sanches and Marques, 2000b). Instead of performing volume reconstruction and image alignment as two separate tasks we perform a joint estimation of alignment and reconstruction parameters. This will be denoted as alignment-by-reconstruction algorithm. The problem is formulated in a Bayesian framework. The estimation of the volume and alignment parameters is achieved by optimizing the same objective function. It is remarked that a different approach is followed in most works: volume reconstruction and image alignment are performed using different criteria (Raya and Udupa, 1990; Tagare, 1999; Dorai et al., 1998; Rohling et al., 1998).

To illustrate the application of the proposed algorithm experimental results obtained by using synthetic and real data are presented. Monte Carlo tests will also be included to evaluate the robustness of the algorithm.

This paper is organized as follows: Section 2 describes the alignment-by-reconstruction algorithm; Section 3 addresses optimization issues; Section 4 presents some experimental results and Section 5 concludes the paper.

2. Alignment-by-reconstruction

Let $f(x)$ be a scalar function describing the volume reflectivity. It is assumed that this function is defined by

$$f(x) = B(x)^{\mathrm{T}} U \tag{1}$$

where $B(x) = [b_1(x), b_2(x), \ldots, b_N(x)]^{\mathrm{T}}$ is a vector of basis functions and $U = [u_1, u_2, \ldots, u_N]^{\mathrm{T}}$ is a $N \times 1$ vector of coefficients (see Sanches and Marques, 2000a for details).

The available data, consists of a sequence of ultrasound images, corresponding to cross-sections of the body, complemented with the information about the position and orientation of the ultrasound probe for each image. In this way, it is possible to know the 3D position of each pixel for each observed image. Therefore, the available data consists of a set $V = \{y_i^p, x_i^p\}$ where y_i^p is the intensity of the ith pixel, x_i^p is a 3D vector with the pixel coordinates and p is the cross-section label.

In this paper a statistical approach is used to estimate the volume. It is assumed that $V = \{y_i^p, x_i^p\}$ is a realization of a set of random variables with a known parametric model which is described in the sequel.

Let x_i^p be the 3D coordinate of the ith pixel on the pth image plane, as before. It will be assumed that x_i^p is corrupted by a translation error parallel to plane associated with the pth cross-section (see Fig. 4). This assumption is adopted for the sake of simplicity but it can be generalized if needed. The measured position of the ith pixel is

$$\hat{x}_i^p = x_i^p + e^p \tag{2}$$

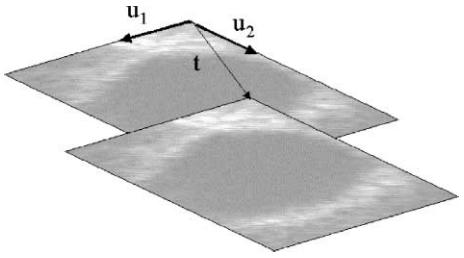

Fig. 4. Cross-section displacement.

where x_i^p is the true pixel position and e^p is the translation error displacement associated to the pth plane.

Let $\bar{u}_x^p$ and $\bar{u}_y^p$ be two unit vectors belonging to the pth cross-section. The translation error can be expressed as

$$e^p = K_x^p \bar{u}_x^p + K_y^p \bar{u}_y^p \tag{3}$$

The alignment algorithm aims to estimate the displacement coordinates (K_x^p, K_y^p) for each observed plane during the volume estimation process. This will be done by the MAP method using the same objective function to estimate the displacements, K, and volume coefficients U. This cost function is the logarithm of the posterior density,

$$\begin{aligned} L(U,K) &= \log p(U,K|V) \\ &= \log(p(V|U,K)p(U)p(K)) + C \end{aligned} \tag{4}$$

where $p(V|U,K)$ is the sensor model, $P(U)$ and $P(K)$ are priors associated to the unknown parameters U and K, respectively, and C is a constant. This constant will be discard because it is not relevant for the maximization process. In (4) it is assumed that U and K are independent random variables. This is a reasonable assumption since the 3D function describing the volume is not related to the measurement error generated by the spatial locator.

The algorithm proposed in this paper consists of two steps, as shown in Fig. 5. In the first step, volume parameters are estimated using the best estimates for the displacement. The volume estimates are then used in the second step to refine the displacement parameters. Both steps alternate during the optimization process until convergence is achieved. Each step of the algorithm corresponds to a maximization of the objective function, L, with respect to one set of unknowns U or

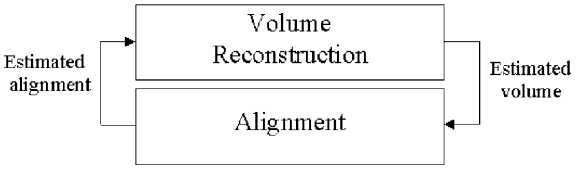

Fig. 5. Estimation process.

K. The proposed algorithm, denoted as alignment-by-reconstruction algorithm is given by

Reconstruction:

$$\widehat{U} = \arg\max_{U} L(U,K) \tag{5}$$

Alignment:

$$\widehat{K} = \arg\max_{K} L(U,K) \tag{6}$$

In this paper, it is assumed that the displacement vectors (K_x^p, K_y^p), are independent and normally distributed with zero mean, i.e., $K \sim N(0,R)$ with $R = \mathrm{diag}\{\sigma_x^2, \sigma_y^2\}$. Therefore the prior is

$$p(K) = \prod_p \frac{1}{2\pi\sigma_x\sigma_y} \mathrm{e}^{-(K_x^p)^2/2\sigma_x^2} \mathrm{e}^{-(K_y^p)^2/2\sigma_y^2} \tag{7}$$

Furthermore, the image pixels are assumed to be independent random variables with Rayleigh distribution (Burckhardt, 1978; Abbot and Thurstone, 1979). This leads to the following model

$$p(V|U,K) = \prod_{i,p} \frac{y_i^p}{f(x_i^p)} \mathrm{e}^{-(y_i^p)^2/2f(x_i^p)} \tag{8}$$

A Gibbs prior is adopted for the volume coefficients (Geman and Geman, 1984)

$$p(U) = \frac{1}{Z}\mathrm{e}^{-\alpha\sum_{(i,j)\in\Gamma} P_i(u_j)} = \frac{1}{Z}\mathrm{e}^{-\alpha\sum_{(i,j)\in\Gamma}(u_i-u_j)^2} \tag{9}$$

where Γ is the set of all pairs of grid indices (i,j) such that $\|x_i - x_j\| \leqslant \Delta$ and Z is a normalization factor (see Sanches and Marques, 2000a, for details). Replacing (7)–(9) in (4) leads to

$$\begin{aligned} L(U,K) = \sum_p \Bigg[\sum_i \left[\log\left(\frac{y_i^p}{f(x_i^p)}\right) - \frac{(y_i^p)^2}{2f(x_i^p)} \right] \\ - \log\left(2\pi\sigma_x\sigma_y\right) - \frac{(K_x^p)^2}{2\sigma_x^2} - \frac{(K_y^p)^2}{2\sigma_y^2} \Bigg] \\ - \log(Z) - \alpha\sum_g (u_g - u_{gi})^2 \end{aligned} \tag{10}$$

The optimization of (10) is addressed in the next section.

3. Optimization procedure

To solve (5) and (6) stationary points of (4) with respect to U and K will be computed. This is a difficult task because the number of unknowns is very high (e.g. $100 \times 100 \times 100$) and (4) is a non-convex function (Li, 1998). To solve this optimization problem numerical methods are needed.

3.1. Volume reconstruction

Eq. (5) is solved by using the ICM algorithm (Besag, 1986), i.e., the optimization will be performed by considering one variable at a time, keeping the others constant. Each uni-dimensional equation is solved by the Newton–Raphson method (Press et al., 1994), leading to

$$\begin{aligned} {}^{n+1}\hat{u}_p = {}^{n}\hat{u}_p \\ + \frac{0.5\sum_i \dfrac{y_i^2 - 2f(x_i)}{f^2(x_i)} b_p(x_i) - 2\alpha N_v(u_p - \bar{u}_p)}{\sum_i \dfrac{y_i^2 - f(x_i)}{f^3(x_i)} b_p^2(x_i) + 2\alpha N_v} \end{aligned} \tag{11}$$

where

$$\bar{u}_p = \frac{1}{N_v}\sum_{u_g\in\delta_p} u_g \tag{12}$$

${}^{n}\hat{u}_p$ is the estimate of u_p at the nth iteration and N_v is the number of control points inside the neighborhood δ_p of the pth grid node $p(N_v = 6)$.

3.2. Alignment

Eq. (6) is also solved by the ICM algorithm, but the displacement coordinates associated with each cross-section are simultaneously estimated. To do that, a multi-dimensional version of the Newton–Raphson algorithm is used:

$$\begin{aligned} {}^{n+1}(K_x^p, K_y^p) = {}^{n}(K_x^p, K_y^p) - \vec{\nabla}L(U,K) \\ \times H(U,K)^{-1} \end{aligned} \tag{13}$$

where $\vec{\nabla}L(U,K)$ is the gradient of L and $H(U,K)$ is the Hessian matrix. The computation of $\vec{\nabla}L(U,K)$ and H leads to

$${}^{n+1}\widehat{K}_x^p = {}^{n}\widehat{K}_x^p\left(1 - \xi_x\frac{L_yL_{xy} - L_xL_{yy}}{L_{xx}L_{yy} - L_{xy}^2}\right) \tag{14}$$

$$ {}^{n+1}\widehat{K}_y^p = {}^{n}\widehat{K}_y^p \left(1 - \xi_y \frac{L_x L_{xy} - L_y L_{xx}}{L_{xx} L_{yy} - L_{xy}^2}\right) \tag{15} $$

where

$$ L_x = \frac{1}{2}\sum_i \left(a_i \frac{\mathrm{d}f(x_i^p)}{\mathrm{d}K_x^p}\right) - \frac{K_x^p}{\sigma_x^p} $$

$$ L_y = \frac{1}{2}\sum_i \left(a_i \frac{\mathrm{d}f(x_i^p)}{\mathrm{d}K_y^p}\right) - \frac{K_y^p}{\sigma_y^p} $$

$$ L_{xx} = -\sum_i \left(b_i \left(\frac{\mathrm{d}f(x_i^p)}{\mathrm{d}K_x^p}\right)^2\right) - \frac{1}{\sigma_x^p} $$

$$ L_{yy} = -\sum_i \left(b_i \left(\frac{\mathrm{d}f(x_i^p)}{\mathrm{d}K_y^p}\right)^2\right) - \frac{1}{\sigma_y^p} $$

$$ L_{xy} = -\sum_i \left(b_i \frac{\mathrm{d}f(x_i^p)}{\mathrm{d}K_x^p}\frac{\mathrm{d}f(y_i^p)}{\mathrm{d}K_y^p}\right) $$

and

$$ a_i = \frac{(y_i^p)^2 - 2f(x_i^p)}{f(x_i^p)^2} $$

$$ b_i = \frac{(y_i^p)^2 - f(x_i^p)}{f(x_i^p)^3} $$

and ξ_x, ξ_y are update gains.

The sums involved in the previous expressions are computed for all pixels belonging to the pth image. The derivatives used in these expression are given by

$$ \frac{\mathrm{d}f(x_i^p)}{\mathrm{d}K_\tau^p} = \frac{\mathrm{d}f(x_i^p)}{\mathrm{d}x_i^p}\frac{\mathrm{d}x_i^p}{\mathrm{d}K_\tau^p} = \vec{\nabla} f(x_i^p)\vec{u_\tau^p} \tag{16} $$

where $\vec{\nabla} f(x_i^p)$ is the gradient of $f(x_i^p)$ computed in x_i^p and $\vec{\nabla} f(x_i^p)\vec{u_\tau^p}$ is the derivative of $f(x_i^p)$ along the $\vec{u}_\tau^p$ direction.

3.3. Initialization

The alignment-by-reconstruction method is initialized as follows. During the first 4 iterations no alignment is performed. The volume coefficients obtained in this way are then used to estimate the displacement errors.

The optimization of the displacement parameters in the initial iteration is performed using a blurred reconstructed volume (initial volume estimate) since no alignment was performed. In this iteration the objective function $L(U,K)$ is smooth as we may observe in Fig. 6d. During the optimization process the volume estimates improve and L becomes sharper (Fig. 6e). Therefore, in the first iterations the algorithm performs a coarse alignment while after a few iterations is able to produce better alignment results.

4. Experimental results

Experimental tests were performed to evaluate the alignment-by-reconstruction algorithm described above. Two types of tests were carried out: tests with synthetic images and with ultrasound images. The former allow to assess the algorithm performance under controlled conditions while the latter illustrate the results achieved in medical reconstruction problems.

4.1. Tests with synthetic images

These tests aim to characterized the performance of the alignment-by-reconstruction algorithm under controlled conditions. A set of 50 images with white Rayleigh noise were used in these experiments. Each image corresponds to a cross-section of a cylinder with radius r shown in Fig. 7a.

Two experiments are described in the sequel. The first is a 2D alignment problem in which all the images are obtained from the same cutting plane, orthogonal to the cylinder axis. The image center and pixels are however different for each image (Fig. 7b). The goal of this experiment is to reconstruct the whole plane from this set of partial and misaligned images.

The coordinates of the image center are modified by a random displacement with normal distribution $N(0,\sigma^2 I)$. The reconstruction was performed for several values of σ^2 and for each value 20 experiments were done. The bias and standard deviation of the alignment errors were computed. It was concluded from these experiments that the displacement estimates are unbiased. The standard deviation of the alignment error is shown in Fig. 8. It is concluded that good alignment is achieved for $\sigma < 0.8r$.

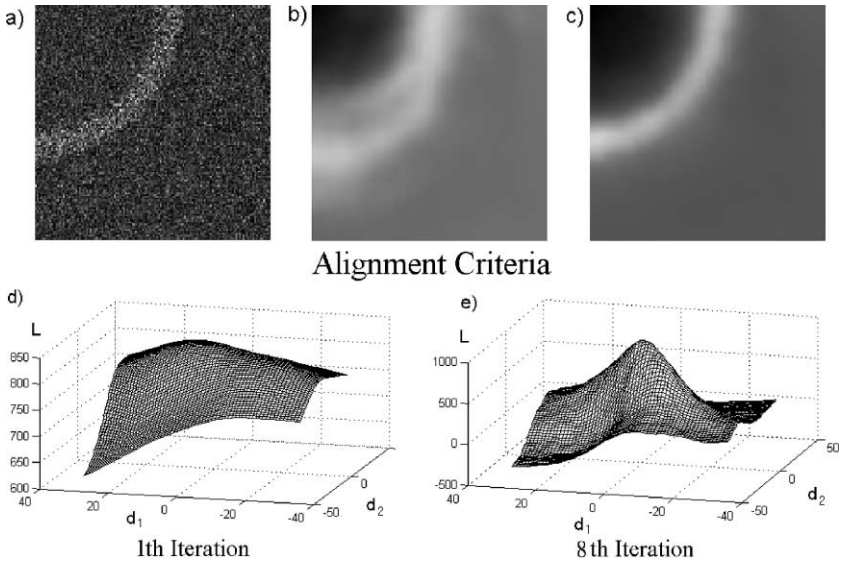

Fig. 6. Alignment-by-reconstruction: (a) original image; (b and c) cross-sections extracted from the initial (b), and final (c), volume estimates; (d and e) objective function $L(U,K)$ in the first (d), and 8th (e), iteration.

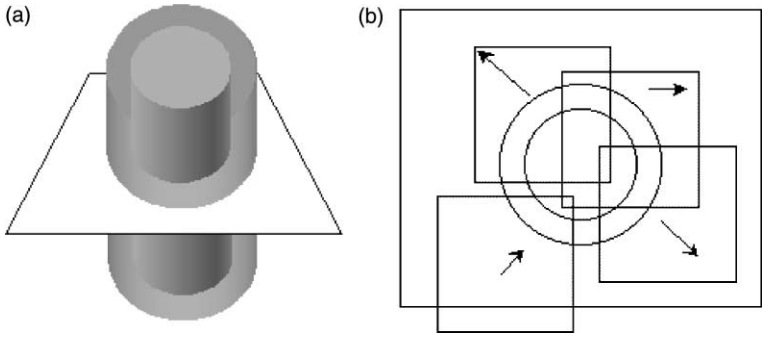

Fig. 7. (a) 3D tube, (b) position errors.

The second experiment aims to reconstruct the cylinder using 100 cross-sections. In this experiment the image center was corrupted by Gaussian displacement $K_p \sim N(0, \sigma^2 I)$.

Fig. 9a shows four images from the data set used to estimate the cylinder. Fig. 9b and c show the reconstruction results obtained without and with alignment. Fig. 10 shows two cross-sections embracing all the volumes of the cylinder obtained by both methods. The improvement obtained by the alignment-by-reconstruction algorithm is clear in both cases.

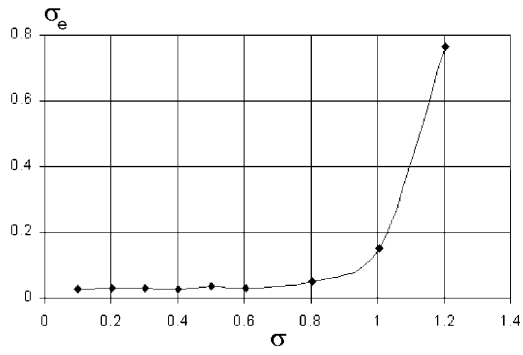

Fig. 8. Standard deviation of the alignment error.

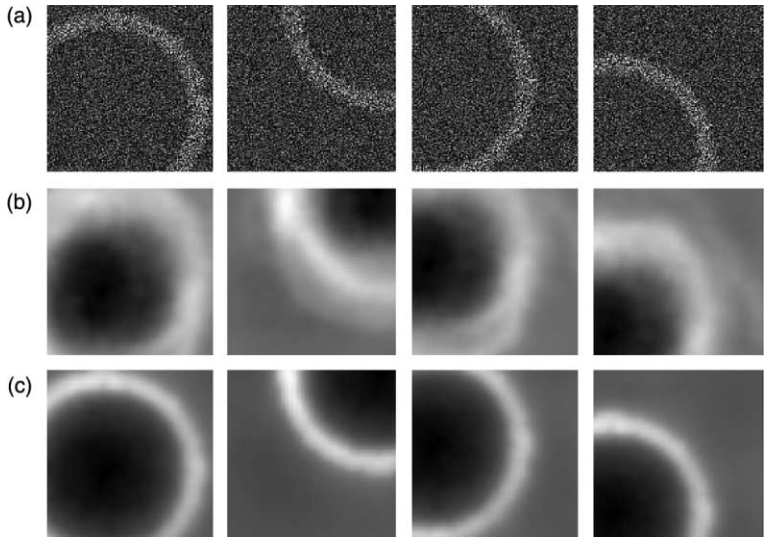

Fig. 9. Reconstruction results with synthetic data (tube).

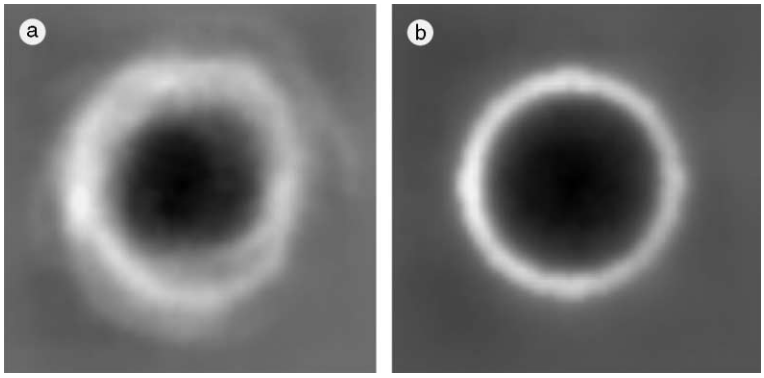

Fig. 10. Cross-sections embracing the reconstructed volume.

In Fig. 11 two rendered surfaces of a 3D cylindrical bar are shown. These results are achieved using both methods (with and without alignment).

4.2. Tests with medical data

To test the algorithm described in this paper with medical data two sets of images corresponding to cross-sections of human organs were used. For each test sequence a subset of five images is shown as well as the corresponding reconstructed cross-sections. For comparison purposes we have also included the reconstruction results obtained

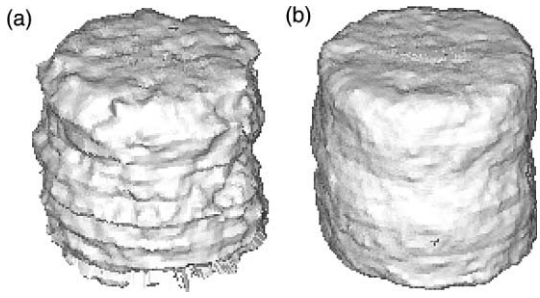

Fig. 11. Reconstruction results of a cylindrical bar without (a) and with (b) alignment.

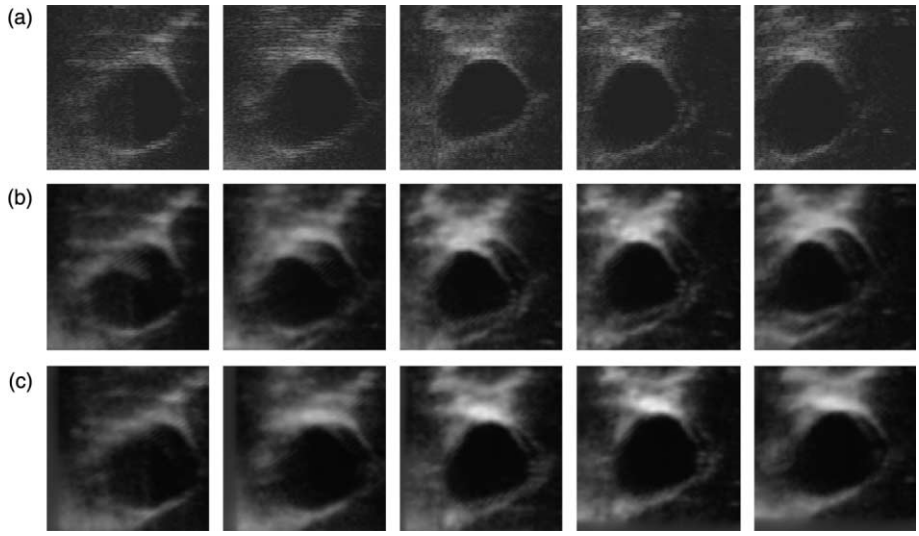

Fig. 12. Reconstruction results of a gall bladder; original images (first row) and cross-sections of the reconstructed volume obtained without alignment (second row) and with alignment (third row).

without alignment. The sequences used correspond to cross-sections of a gall bladder (Fig. 12) and a thyroid (Fig. 13). A cross-section of the whole estimated volume is also shown for the case of a gall bladder (Fig. 14). It is remarked that the alignment-by-reconstruction algorithm manages to reduce the artifacts which can be observed in the results obtained without alignment. These artifacts do not correspond to any anatomic detail but they are produced by image misalignment.

When the misalignment is strong, as in the gall bladder experiment (Fig. 12b), the same boundary may appear several times in the reconstructed cross-sections. When the misalignment is smaller

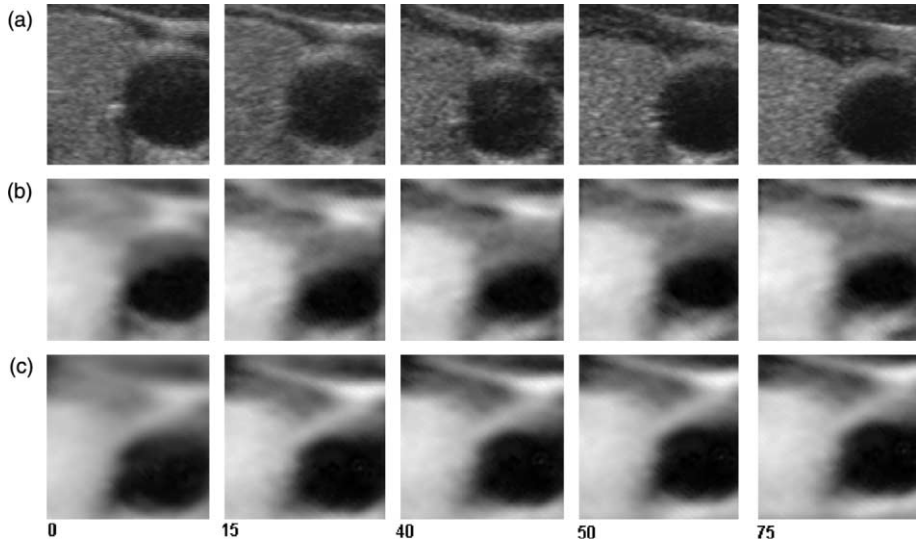

Fig. 13. Reconstruction of a thyroid: (a) original image (first row); (b) reconstructed cross-sections without alignment (second row) and (c) with alignment (third row).

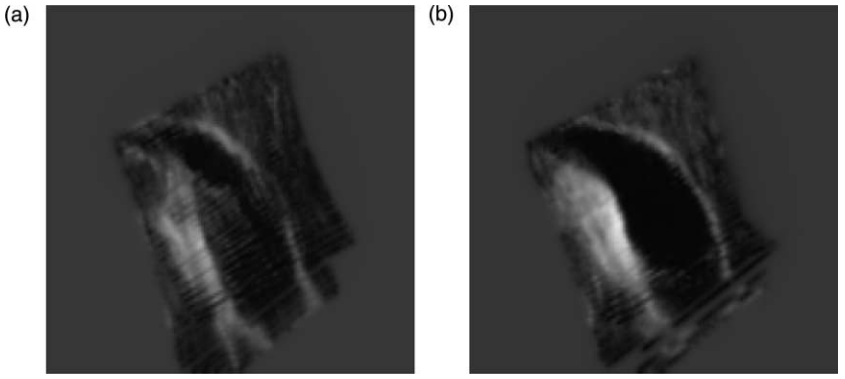

Fig. 14. Volume reconstruction from a gall bladder. Cross-sections embracing all the volume.

the estimated volume is blurred as it happens in the case of the thyroid (Fig. 12b).

5. Conclusion

This paper addresses volume reconstruction from a set of ultrasound images when the probe position and orientation cannot be accurately measured. Position and orientation errors produce a significant degradation of the reconstruction results, often perceived as a blur effect. To overcome this difficulty an image alignment method is proposed.

Instead of performing volume reconstruction and image alignment in two separate steps, a joint estimation of volume and alignment parameters is described in this paper. Both steps alternate during the reconstruction process using a single objective function. This avoids the use of different and some times incompatible strategies in alignment and volume estimation.

The experimental results presented in the paper show that significant improvements are achieved by performing the dynamic alignment of the observed images during the reconstruction process.

References

Anderson, J.M.M., 1997. Weighted least-square reconstruction methods for positron emission tomography. IEEE Trans. Med. Imaging 16 (2), 159–165.

Abbot, J., Thurstone, F., 1979. Acoustic speckle: theory and experimental analysis. Ultrasound Imaging 1, 303–324.

Besag, J., 1986. On the statistical analysis of dirty pictures. J. Roy. Statist. Soc. B 48 (3), 259–302.

Burckhardt, C., 1978. Speckle in ultrasound B-mode scans. IEEE Trans. Sonics Ultrasonics SU-25 (1), 1–6.

Carr Jonathan, 1996. Surface reconstruction in 3D medical imaging. Ph.D. Thesis. University of Canterbury.

Dorai, C., Wang, G., Jain, A.K., Mercer, C., 1998. Registration and integration of multiple object views for 3D model construction. IEEE Trans. PAMI 20 (1), 83–89.

Geman, S., Geman, D., 1984. Stochastic relaxation, gibbs distributions, and the bayesian restoration of images. IEEE Trans. Pattern Anal. Mach. Intell., PAMI 6 (6), 721–741.

Green, P.J., 1990. Bayesian reconstructions from emission tomography data using a modified em algorithm. IEEE Trans. Med. Imaging 9 (1), 84–93.

Herman, G.T., Kuba, A., 1999. Discrete Tomography, Foundations, Algorithms, and Applications, Birkhauser.

Li, S.Z., 1998. Close-form solution and parameter selection for convex minimization-based edge-preserving smoothing. IEEE Trans. PAMI 20 (9), 916–932.

Nelson, T.R., Downey, D., Pretorius, D., Fenster, A., 1999. Three-Dimensional Ultrasound, Lippincott.

Nelson, T.R., Pretorius, D.H., 1997. Interactive acquisition, analysis and visualization of sonographic volume data. Int. J. Imaging Syst. Technol. 8, 26–37.

Ogawa, S., et al., 1998. Three dimension ultrasonic imaging for diagnosis of beast tumor. Proceedings of British Machine Vision Conference, Edinburgh, pp. 1677–1680.

Press, W.H., Vetterling, W.T., Teukolsky, S.A., Flanner, B.P., 1994. Numerical recipes in C. Cambridge University Press.

Quistgaard, J., 1997. Signal acquisition and processing in medical diagnostics ultrasound. IEEE Signal Process. Mag. 14 (1), 67–74.

Raya, S.P., Udupa, J.K., 1990. Shape-based interpolation of multidimensional objects. IEEE Trans. Med. Imaging 9 (1), 3–42.

Rohling, R.N., Gee, A.H., Berman, L., 1999. A comparison of freehand three-dimensional ultrasound reconstruction techniques. Med. Image Anal. 4 (4), 339–359.

Rohling, R.N., Gee, A.H., Berman, L., 1998. Automatic registration of 3-D ultrasound images. Ultrasound Med. Biol. 24 (6), 841–854.

Sanches, J., Marques, J., 2000a. A Rayleigh reconstruction/interpolation algorithm for 3D ultrasound. Pattern Recogn. Lett. 21, 917–926.

Sanches, J., Marques, J., 2000b. Alignment-by-reconstruction for 3D ultrasound imaging. Proceedings of ICPR2000, Barcelona, vol. 3, pp. 41–44.

Tagare, H.D., 1999. Shape-based nonrigid correspondence with application to heart motion analysis. IEEE Trans. Med. Imaging 18 (7), 570–579.